AIAA JOURNAL
Vol. 47, No. 4, April 2009

Modeling Rotor Wake Dynamics with Viscous Vortex Particle Method

Chengjian He* and Jinggen Zhao†
Advanced Rotorcraft Technology, Inc., Mountain View, California 94043

DOI: 10.2514/1.36466

Rotor-induced-flow modeling and prediction has been one of the central issues for rotorcraft performance, control, stability, loads, and vibration analysis for decades. Traditional singularity-based methods used in most current comprehensive rotorcraft analysis codes are limited by the potential flow assumption and thus have to rely on empirical formulations (e.g., vortex decay factor, vortex core size, etc.) to reach a solution. This paper discusses the development and validation of a viscous vortex particle model for modeling the complicated rotor wake vorticity transportation and diffusion. Instead of solving the viscous vorticity equations through numerical discretization over the flowfield grid, the vortex particle method addresses the solution through a Lagrangian formulation in which there is no artificial numerical dissipation involved. The Lagrangian approach also allows the application of the hierarchical TreeCode and the fast multipole method. These methods can dramatically improve the computational efficiency of the viscous vortex particle simulation, which enables it to be used for practical and comprehensive rotorcraft analysis.

Nomenclature

C_T	=	rotor thrust coefficient
c_σ	=	vortex particle overlapping parameter
h_{res}	=	flowfield resolution parameter
$\mathbf{L}$	=	rotor blade segment circulation lift per unit length
N	=	number of vortex particles
NAZ	=	number of integration steps per one rotor revolution
N_{rev}	=	number of rotor revolutions
R	=	rotor radius
r	=	radial position along the blade span
r_{cut}	=	rotor wake cutoff distance
$\mathbf{u}$	=	velocity field
V_i	=	volume of the ith vortex particle
V_z	=	wake-induced downwash
$\mathbf{v}_b$	=	resultant air velocity relative to blade segment
$\mathbf{x}$	=	vortex particle displacement vector
x	=	longitudinal displacement from the rotor hub center
y	=	lateral displacement from the rotor hub center
z	=	vertical displacement from the rotor hub center
$\boldsymbol{\alpha}$	=	total vorticity of a vortex particle
$\boldsymbol{\alpha}_0$	=	initial value of total vorticity ($\boldsymbol{\alpha}$)
Γ_b	=	rotor bound circulation
$\boldsymbol{\gamma}_w$	=	rotor wake vorticity source
μ	=	rotor advance ratio
ν	=	kinematic viscosity
ξ	=	vorticity distribution function
ρ_{air}	=	air density
σ	=	smoothing parameter ($c_\sigma h_{\text{res}}$)
ψ	=	rotor azimuth
$\boldsymbol{\omega}$	=	vorticity field
∇^2	=	Laplacian operator

Subscripts

i, j	=	particle index
PSE	=	particle strength exchange
ST	=	stretching

I. Introduction

DUE to the complexity of rotor wake dynamics, rotor downwash analysis remains one of the most challenging tasks for rotor aerodynamics modeling. Under hover and low-speed flight conditions, the rotor wake remains in the vicinity of the operating rotor blades. The close interaction of the rotor wake with the rotor blades has a strong impact on the variation of the rotor blade airloads. In hover, over 60% of the rotorcraft power is due to the rotor-induced power. The rotor wake is a major cause of the vehicle vibration in hover and low-speed forward flight. The rotor wake also presents a hazardous environment when the vehicle is operating near the ground. A strong rotor downwash near a ground surface can blow away ground objects and put ground personnel in a dangerous situation. This is especially true for heavy-lift helicopters or tiltrotors with high rotor disk loading. The rotor/airframe/empennage interaction is another complicated aerodynamic problem that remains a challenging subject due to the fact that it strongly affects rotorcraft handling qualities and, unfortunately, is very difficult to analytically predict and simulate.

Most current comprehensive rotorcraft analysis codes adopt singularity-based methods for the rotor wake solution. These singularity-based methods typically use singularities such as a lifting line to represent the rotor blade, a system of vortices to represent the rotor wake (e.g. free wake models), and a set of source/doublet panels to model the fuselage. Although these singularity methods are computationally efficient, they are only able to capture the first-order effects, due to the potential flow assumption, and therefore have to rely on an empirical formulation (e.g., vortex decay factor, vortex core size, etc.) for the rotor wake solution. The rotorcraft fuselage is typically modeled using a panel method that renders the calculation of some aerodynamic interaction effects, such as flow separation due to rotor downwash, extremely difficult. In cases in which viscous effects are dominant, the viscous effects must either be ignored, prespecified, or determined by coupling the method to a boundary-layer-type model, which makes this method inaccurate.

There has been promising progress in modeling techniques for rotor wake dynamics solution in recent years, but most of them are currently still not efficient enough to accurately predict the rotorcraft

Presented as Paper 0339 at the 46th AIAA Aerospace Sciences Meeting and Exhibit, Reno, NV, 7–10 January 2008; received 4 January 2008; revision received 15 December 2008; accepted for publication 22 December 2008.

*Vice President, Research and Development. Senior Member AIAA.
†Senior Scientist. Member AIAA.

aerodynamics. The major deficiencies of currently used modeling techniques are their inability to accurately predict the rotor wake geometry and the variation of the wake vorticity strength during the wake transportation. The most challenging issue for rotor wake modeling and simulation is to preserve the concentrated vorticity over a long distance and/or significant periods of time without much numerical dissipation and diffusion, while retaining the physical diffusion and dissipation caused by viscosity and turbulence to correctly simulate the wake decay. Most current Navier–Stokes computational fluid dynamics (CFD) methods solve the flow dynamics equations through numerical discretization (e.g., finite difference), which inherently suffers from excessive dissipation due to the numerical discretization and causes the tip vortices to be captured with much less intensity than the physical reality.

To overcome the hurdle of artificial numerical dissipation that is inherent in most current Navier–Stokes CFD methods, a vorticity transportation model, which uses a mixed Eulerian/Lagrangian method and an adaptive-grid system to increase the grid resolution, has been used to address the problem by solving the fluid dynamics equations in vorticity conservation form [1,2]. Instead of solving the viscous vorticity equations through numerical discretization over the flowfield grid, the current research adopts a viscous vortex particle method, which provides a natural and more promising solution for simulating the rotor blade vorticity transportation and interaction.

The vortex particle method addresses the solution via a grid-free Lagrangian formulation in which there is no artificial numerical dissipation involved. Although modeling the vorticity diffusion in viscous flow presents a great challenge to most grid-based numerical simulations, the vortex particle method can easily accommodate the effect of air viscosity on physical diffusion in the simulation. The results of numerous investigations on the vortex particle method for both two-dimensional and three-dimensional viscous flows have appeared in the literature [3–10], which have greatly enriched our understanding of the general vortex particle modeling methodology. The current research was focused on the formulation development and numerical simulation of the challenging unsteady rotor wake problem. In addition, the Lagrangian approach allows the application of the hierarchical TreeCode and the fast multipole method [11–17], which can significantly improve the computational efficiency for the vortex particle method to be used for comprehensive rotorcraft analysis.

II. Viscous Vortex Particle Model

A. Vorticity Dynamics Equation

The Navier–Stokes equation for incompressible air can be expressed in either an Eulerian description (primitive form) or a vorticity velocity form with a Lagrangian description. The viscous vortex particle method adopts the Lagrangian description of the vorticity velocity form, which gives the vorticity dynamics equation as follows:

$$\frac{d\boldsymbol{\omega}}{dt} = \boldsymbol{\omega} \cdot \nabla \mathbf{u} + \nu \nabla^2 \boldsymbol{\omega} \tag{1}$$

where $\boldsymbol{\omega} = \nabla \times \mathbf{u}$ is the vorticity field associated with the velocity field $\mathbf{u}$,

$$\frac{d(\,)}{dt} = \frac{\partial(\,)}{\partial t} + \mathbf{u} \cdot \nabla(\,)$$

is the material derivative, and ν is the kinematic viscosity.

The vorticity velocity form with a Lagrangian description is a natural means of solving the vortex wake transport problem. The vortex particle model based on the vorticity velocity formulation does not require any grid generation, which offers an advantage over the finite difference approach, in which the grid generation is a large undertaking for practical engineers. In addition, the convection term in Eq. (1) is not treated explicitly, which renders a dissipation-free scheme for the vortex particle model.

B. Vortex Particle Representation

To solve the governing equation (1), the vorticity field is represented by a set of N Lagrangian vector-valued particles as

$$\boldsymbol{\omega}(\mathbf{x}, t) = \sum_{i=1}^{N} \xi_\sigma(\mathbf{x} - \mathbf{x}_i)\boldsymbol{\alpha}_i = \sum_{i=1}^{N} \xi_\sigma(\mathbf{x} - \mathbf{x}_i)\boldsymbol{\omega}_i V_i \tag{2}$$

where $\mathbf{x}_i$ and $\boldsymbol{\alpha}_i$ are the position and the vector-valued total vorticity inside particle i (with volume V_i), respectively; $\xi_\sigma(\mathbf{x}) = \xi(|\mathbf{x}|)/\sigma^3$ (with ξ being the distribution function); and σ is the smoothing parameter, which is the product of the particle overlapping parameter c_σ and the resolution parameter h_{res} (which governs the minimum flowfield resolution). A minimum value of 1.0 for the overlapping parameter is required for solution convergence [4,7,9,10]. Generally speaking, there is a wide range of distribution functions available [5,6]. The Gaussian distribution is used here throughout and the distribution function can then be written as

$$\xi(\rho) = \frac{1}{(2\pi)^{3/2}} e^{-\rho^2/2} \tag{3}$$

With the preceding discrete particle representations (2), the governing equation for the viscous vortex particle model can be rewritten as

$$\frac{d\boldsymbol{\alpha}}{dt} = \boldsymbol{\alpha} \cdot \nabla \mathbf{u} + \nu \nabla^2 \boldsymbol{\alpha} \qquad \boldsymbol{\alpha}(\mathbf{x}, 0) = \boldsymbol{\alpha}_0$$
$$\mathbf{u} = -\sum_{j=1}^{N} \frac{1}{\sigma_j^3} K(\rho)(\mathbf{x} - \mathbf{x}_j) \times \boldsymbol{\alpha}_j \tag{4}$$

where $\rho = |\mathbf{x} - \mathbf{x}_j|/\sigma_j$ is the nondimensional distance parameter. Here, the velocity field corresponding to the vorticity field in Eq. (2) is computed from the convolution of the vorticity field. $K(\rho) = [G(\rho) - \xi(\rho)]/\rho^2$ is the Bio–Savart kernel for the velocity evaluation, and $G(\rho)$ is Green's function for the vector stream function, which can be expressed as

$$G(\rho) = \frac{1}{4\pi\rho} \operatorname{erf}\left(\frac{\rho}{\sqrt{2}}\right)$$

where

$$\operatorname{erf}(s) = 2\int_0^s e^{-v^2} \frac{dv}{\sqrt{\pi}}$$

is the error function.

For the preceding formulation, the convergence of the vortex particle method was proved for both a uniform smoothing parameter [4,9,10] and a varying-size smoothing parameter [7], provided that the overlapping parameter satisfies $c_\sigma \geq 1$.

C. Vortex Particle Convection

The particle positions $\mathbf{x}_i(t)$ are governed by the convection equation as

$$\frac{d\mathbf{x}_i}{dt} = \mathbf{u}(\mathbf{x}_i, t) \tag{5}$$

with the particle velocity defined by

$$\mathbf{u}(\mathbf{x}_i, t) = -\sum_{j=1}^{N} \frac{1}{\sigma_{ij}^3} K(\rho)(\mathbf{x}_i - \mathbf{x}_j) \times \boldsymbol{\alpha}_j \tag{6}$$

where a symmetrized smoothing parameter

$$\sigma_{ij} = \frac{\sqrt{\sigma_i^2 + \sigma_j^2}}{\sqrt{2}}$$

is used to best conserve the linear and angular vortex impulse. The current vortex particle method with N Lagrangian particles is similar

to the traditional N-body problem. If a direct summation method is used, the characteristic speed is $\mathcal{O}(N^2)$. When the particle number N is large, it is very expensive to calculate the velocity field by direct summation of the contributions from all vortex particles. Therefore, a fast summation method is needed to efficiently compute the velocity field due to N particles, which is described in later sections.

D. Vortex Stretching Effect

In the governing equation (1) for the vortex dynamics, the first term in the right-hand side of the equation, $(\boldsymbol{\omega}\cdot\nabla)\mathbf{u}$, is the stretching-effect term, which describes the vortex stretching and rotation due to the velocity gradient. The second term in the right-hand side of the equation is the viscous diffusion term, which describes the vorticity diffusion due to viscous effects.

In the current simulation, the vortex stretching effect is accounted for by using the so-called direct scheme, which directly multiplies the velocity gradient matrix with the particle vorticity as follows:

$$\left.\frac{d\boldsymbol{\alpha}_i}{dt}\right|_{\mathrm{ST}} = [\nabla\mathbf{u}(\mathbf{x}_i,t)]\cdot\boldsymbol{\alpha}_i \tag{7}$$

where the velocity gradient can be obtained by analytically differentiating the velocity field. The induced velocity at particle i [Eq. (6)] can be rewritten into a matrix form as

$$\mathbf{u}(\mathbf{x}_i,t) = \sum_{j=1}^{N}\frac{1}{\sigma_{ij}^3}[\tilde{\boldsymbol{\alpha}}_j][K(\rho)(\mathbf{x}_i-\mathbf{x}_j)] \tag{8}$$

where $[\tilde{\boldsymbol{\alpha}}_j]$ is the skew-symmetric matrix spanned by vector $\boldsymbol{\alpha}_j$. The velocity gradient can then be obtained by differentiating the preceding expression with respect to variable $\mathbf{x}_i$ as

$$\nabla\mathbf{u}(\mathbf{x}_i,t) = \sum_{j=1}^{N}\frac{1}{\sigma_{ij}^3}[\tilde{\boldsymbol{\alpha}}_j][\nabla(K(\rho)(\mathbf{x}_i-\mathbf{x}_j))] \tag{9}$$

For the kl component (k is the row index and l is the column index) of the matrix $[\nabla(K(\rho)(\mathbf{x}_i-\mathbf{x}_j)]$, the following expressions can be attained by chain rule of differentiation:

$$[\nabla(K(\rho)(\mathbf{x}_i-\mathbf{x}_j))]_{kl} = \frac{\partial K(\rho)}{\partial x_{i_k}}(x_{i_l}-x_{j_l}) + K(\rho)\frac{\partial(x_{i_l}-x_{j_l})}{\partial x_{i_k}} \tag{10}$$

Note that the second term is nonzero only when $k=l$. By applying the relationship

$$\rho = \frac{|\mathbf{x}_i-\mathbf{x}_j|}{\sigma_{ij}} = \sqrt{\sum_{l=1}^{3}(x_{i_l}-x_{j_l})^2}$$

it can be shown that

$$\frac{\partial K(\rho)}{\partial x_{i_k}} = \frac{\partial K(\rho)}{\partial\rho}\frac{\partial\rho}{\partial x_{i_k}} = \frac{1}{\sigma_{ij}^2}\frac{\partial K(\rho)}{\partial\rho}\frac{(x_{i_k}-x_{j_k})}{\rho} \tag{11}$$

Using the definition for the velocity kernel

$$K(\rho) = \frac{G(\rho)-\xi(\rho)}{\rho^2}$$

and the chain rule of differentiation gives rise to the following expression for $\partial K(\rho)/\partial\rho$:

$$\frac{\partial K(\rho)}{\partial\rho} = -2\frac{G(\rho)-\xi(\rho)}{\rho^3} + \frac{1}{\rho^2}\left(\frac{\partial G(\rho)}{\partial\rho}+\frac{\partial\xi(\rho)}{\partial\rho}\right) \tag{12}$$

By the definitions of the Green and Gaussian kernels $G(\rho)$ and $\xi(\rho)$, it can be shown that

$$\frac{\partial G(\rho)}{\partial\rho} = -\frac{G(\rho)-\xi(\rho)}{\rho} \tag{13}$$

$$\frac{\partial\xi(\rho)}{\partial\rho} = \rho\xi(\rho) \tag{14}$$

Substituting Eqs. (13) and (14) into Eq. (11) and the resulting equation into Eq. (10) gives rise to

$$[\nabla(K(\rho)(\mathbf{x}_i-\mathbf{x}_j))]_{kl} = \delta_{kl}K(\rho) - \frac{1}{\sigma_{ij}^2}F(\rho)(x_{i_k}-x_{j_k})(x_{i_l}-x_{j_l}) \tag{15}$$

where the kernel

$$F(\rho) = \frac{3K(\rho)-\xi(\rho)}{\rho^2}$$

Note that the calculation of the velocity gradient by direct summation of the contributions from all N particles is similar to that in the velocity evaluation, which requires an $\mathcal{O}(N^2)$ computational cost. Therefore, the fast method used in the velocity evaluation will also be used to evaluate the velocity gradient when the target point is far away from the source.

E. Viscous Diffusion Effect

The second term, $\nu\nabla^2\boldsymbol{\omega}$, in the right-hand side of the vorticity governing equation (1) is the viscous diffusion term. The viscous diffusion term describes the effects of air viscosity throughout the vorticity transportation. In this study, the particle strength exchange (PSE) method [4,6–8,10,18] is used to solve for the viscous diffusion effect. The fundamental approach of the PSE algorithm is to approximate the Laplacian operator ∇^2 with an integral operator, thus avoiding any numerical differentiation, which has a poor numerical accuracy when compared with the integral operation. The approximation can be written as [4,10,18]

$$\nabla^2\boldsymbol{\omega}(\mathbf{x}) \approx \frac{2}{\sigma^2}\int\eta_\sigma(\mathbf{x}-\mathbf{y})[\boldsymbol{\omega}(\mathbf{y})-\boldsymbol{\omega}(\mathbf{x})]\mathrm{d}\mathbf{y} \tag{16}$$

provided that the kernel η_σ satisfies the moment conditions. In the PSE algorithm, the kernel η_σ was the same as the Gaussian distribution in Eq. (3). The preceding integral can be discretized by midpoint quadrature over all the particles, which results in the following operator:

$$\nabla^2\boldsymbol{\omega}(\mathbf{x}) \approx \frac{2}{\sigma^2}\sum_j\eta_\sigma(\mathbf{x}-\mathbf{y}_j)[\boldsymbol{\omega}_j(\mathbf{y}_j)-\boldsymbol{\omega}(\mathbf{x})]V_j \tag{17}$$

Integrating Eq. (17) over the volume V_i of particle i yields

$$\int_{V_i}\nabla^2\boldsymbol{\omega}(\mathbf{x})\mathrm{d}\mathbf{x} \approx \frac{2}{\sigma^2}\sum_j\int_{V_i}\eta_\sigma(\mathbf{x}-\mathbf{y}_j)[\boldsymbol{\omega}_j(\mathbf{y}_j)-\boldsymbol{\omega}(\mathbf{x})]V_j\mathrm{d}\mathbf{x} \tag{18}$$

Applying the midpoint quadrature rule to the preceding integral gives rise to (after substituting $\boldsymbol{\alpha}_i=\boldsymbol{\omega}_iV_i$ and $\boldsymbol{\alpha}_j=\boldsymbol{\omega}_jV_j$)

$$\int\nabla^2\boldsymbol{\omega}(\mathbf{x})\mathrm{d}\mathbf{x} \approx \frac{2}{\sigma^2}\sum_j\eta_\sigma(\mathbf{x}_i-\mathbf{y}_j)(V_i\boldsymbol{\alpha}_j - V_j\boldsymbol{\alpha}_i) \tag{19}$$

The rapid decrease of the kernel η_σ indicates that only the particles close to particle i contribute significantly to the PSE for $d\boldsymbol{\alpha}_i/dt$. Therefore, only a subset P_i of all the particles needs to be considered. Therefore, the final expression for the viscous diffusion effect can be formulated as

$$\left.\frac{d\boldsymbol{\alpha}_i}{dt}\right|_{\mathrm{PSE}} = \frac{2\nu}{\sigma_{ij}^2}\sum_{j\in P_i}(V_i\boldsymbol{\alpha}_j - V_j\boldsymbol{\alpha}_i)\eta_{\sigma_{ij}}(\mathbf{x}_i-\mathbf{x}_j) \tag{20}$$

where a symmetrized smoothing parameter σ_{ij} is used. Because of the skew-symmetric property of the preceding formula, it can be observed that the PSE scheme is conservative, because the vorticity

lost at particle i during its interaction with particle j will be recovered by that gained at particle j.

F. TreeCode and Fast Multipole Method

As described in the previous sections, the particle convection velocity and velocity gradient require the summation of contributions from N particles. For the N-body problem, two major categories of fast summation methods have been discussed in the literature. One is the so-called TreeCode method [11–15] and the other is the fast multipole method (FMM) [16,17]. Both of these algorithms require the generation of a data structure, usually in the form of an Oct-Tree (Quad-Tree for 2-D). The two algorithms differ from each other mainly in how the tree is traveled and how the velocity evaluation is handled.

In the TreeCode algorithm, the influence of a source cell (cluster or group of particles) on a target particle is obtained through multipole expansion if the distance between them is larger than the cell's critical distance. In the FMM method, if two cells are far away from each other, the influence of the source cell on the center of the target cell is first expanded as a multipole series. This multipole series is then transformed into a local Taylor series inside the target cell, and the velocities on all the particles inside the target cell can be quickly evaluated by summing up the local Taylor expansions. In general, the TreeCode algorithm will have a characteristic speed of $\mathcal{O}(N \log N)$, whereas the FMM algorithm will have a characteristic speed of $\mathcal{O}(N)$. However, the FMM approach is more complicated and requires more memory when performing operations.

In this study, both the TreeCode and the FMM algorithms were implemented. The FMM can be used to calculate the particle velocity, the velocity gradient, and the viscous diffusion, and the TreeCode algorithm can be used to calculate the interference velocities on other field points.

III. Rotor Wake Modeling

Unlike a conventional fixed-wing aircraft, which relies on separate mechanisms of generating lift, forward propulsion, and control, a rotorcraft mainly uses the rotors via their rotating blades to provide all three in helicopter mode. The rotors produce aerodynamic forces through the relative motion of the rotor blade surfaces with respect to the air. Because of the rotation, the rotor blades typically experience a strong unsteady variation in their airloads, even in a steady forward-flight condition. The unsteady variation of the blade airloads results in both shed and trailed vorticity emanated into the rotor wake, which creates a complicated aerodynamic environment that the rotors encounter on a continuous basis.

In the viscous vortex particle model, the vorticity originates from the physical body boundaries, such as the rotor blade and the body surfaces. For vortex particle simulation, each aerodynamic surface in the flowfield of interest is treated as a vorticity source that generates the vortex particles for the vorticity transportation simulation. For a lifting rotor operating in free air, the blade surface vorticity is the only source that sheds the vorticity into the rotor wake. To facilitate discussion, Fig. 1 shows the rotor hub reference coordinate system used for the rotor vortex particle simulation (positive x pointing downstream, positive z pointing upward, and positive y formed by the right-hand rule).

Depending on the applications, the rotor blade surface can be represented as a lifting line, a lifting surface, or a more sophisticated CFD formulation. In this study, the interface of the vortex particle model was formulated to interact with lifting-line blades. There is no barrier for this particle model to interface with a lifting surface or a 3-D CFD rotor simulation of a later time. In the lifting-line representation, the blade is discretized into a number of aerodynamic segments. The airloads acting on each blade segment are computed using the local angle of attack, Mach number, and dynamic pressure. The calculation of both the angle of attack and the dynamic pressure includes the effect of the rotor wake-induced velocity derived from the vortex particle simulation. Therefore, the rotor wake and the rotor blade airloads are fully coupled to form a closed-loop solution.

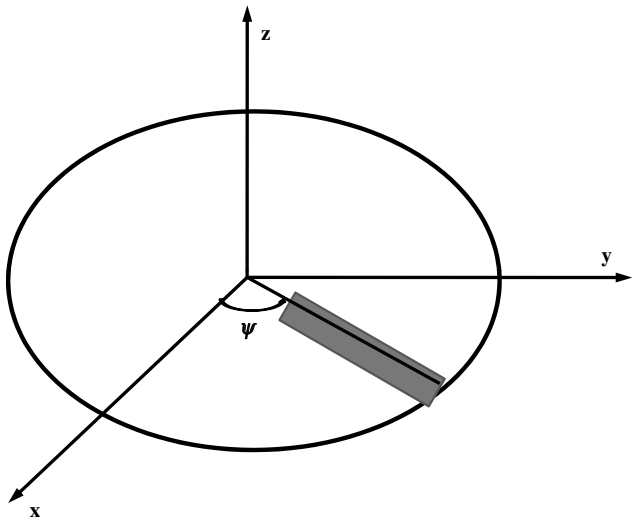

Fig. 1 Rotor hub reference coordinates.

From the lifting-line airloads solution, the blade bound circulation can be computed using the Kutta–Joukowski theorem:

$$\mathbf{L} = \rho_{\text{air}} \mathbf{v}_b \times \Gamma_b \tag{21}$$

where $\mathbf{L}$ is the blade circulation lift per unit length, and Γ_b is the blade bound-circulation vector. The local velocity of the bound circulation relative to the fluid, $\mathbf{v}_b$, is the resultant relative air velocity calculated as the vector sum of the blade structural motion, the ambient wind, the wake-induced velocity, and the interference velocities from other sources.

Because the number of blade aerodynamic segments for the vortex particle simulation is very large, it is reasonable to assume a constant bound circulation over each blade segment. The bound circulation of blade segments usually varies both azimuthally and spanwise. This generates both shed and trailed vortices in the rotor wake. For a conserved-vorticity variation, the vorticity source created at each blade segment and shed into the rotor wake can be written as

$$\boldsymbol{\gamma}_w = -\frac{d\Gamma_b}{dt} + \mathbf{v}_b \nabla \cdot \Gamma_b \tag{22}$$

In the preceding lifting-line vorticity source equation, the first term is the shed vorticity and the second term is the trailed vorticity from each of the blade segments.

In the vortex particle model, new vortex particles are generated behind each rotor blade to account for the blade bound-vorticity changes. The total vorticity source generated from the changes of lifting-line bound circulation at each time step is distributed onto an interpolation surface representing the convected trajectory of the blade during that time step. Usually, the blade spanwise discretization for aerodynamics adopts an equal annulus area rule, which clusters grids toward the blade tip. With a highly dense spanwise discretization, there can be some segments toward the blade tip for which the length is much smaller than the minimum flowfield resolution h_{res}, resolved by the vortex particle simulation. Therefore, to minimize the dependency of the vorticity source generation on the blade spanwise discretization for blade-airload calculation, it would be very desirable to have two sets of blade segment nodes: one set for the blade-airload consideration and the other set for the purpose of vorticity source generation. The two sets of grids are independent of each other geometrically, but correlate with the physical blade span geometry.

To ensure the accuracy of the dual-set-blade grid approach, the blade bound circulation at the aerodynamic segment nodes must be properly interpolated onto the vorticity source segment nodes. In addition, the interpolation must precisely preserve the original shape of the bound-circulation distribution obtained from the segment aerodynamics calculations and not introduce any spurious wiggles or

bumps. In the current study, the piecewise cubic Hermite interpolation algorithm (PCHIP) [19] was adopted. The reason for selecting the PCHIP algorithm instead of other popular algorithms, such as B-spline, is that the PCHIP algorithm precisely preserves the monotonic interpolation property and the original shape of the data.

The azimuthal and spanwise changes of the blade bound circulation continuously generate new vortex particles that are shed into the rotor wake. The vorticity variation of the vortex particles throughout the rotor wake is governed by the fluid physics law, as given in Eq. (1). To improve the computational efficiency, the vortex particles far away from the flowfield area of interest (such as the rotor disk), specified by a wake cutoff distance, will be deleted. The influence of this wake cutoff distance on the simulation fidelity will be examined later through a series of sensitivity studies.

IV. Results and Discussion

To validate the viscous vortex particle model thus developed, simulation results were obtained and compared with the available experimental data for different rotor configurations in both hover and forward flight. Excellent correlations were achieved. The sensitivity of the solution accuracy to modeling parameters [such as the smoothing parameter $\sigma = c_\sigma h_{\text{res}}$, the simulation time-step size (equivalent to NAZ), and the wake cutoff distance r_{cut}] was also investigated through a series of parametric studies. In all of the following simulations (unless otherwise explicitly specified), each blade was discretized into 50 aerodynamic segments and $NAZ = 96$ was used for time integration, which corresponds to a step size of 3.75 deg of rotor azimuth. In addition, the rotor wake cutoff distance was $r_{\text{cut}} = 3.0R$, and the particle overlapping and resolution parameters were $c_\sigma = 1.3$ and $h_{\text{res}} = 0.025R$, respectively.

A. Far-Wake Surveys for a Full-Scale Rotor in Hover

In the first test case, the viscous vortex particle model was applied to simulate the rotor wake vorticity variation and the wake-induced downwash for a two-bladed full-scale rotor in hover. The measurement of the wake-induced velocities below and downstream of the rotor was obtained by Boatwright [20]. During the experiment, the rotor system was mounted on a 60 ft rotor test tower and the measurement consisted of two disk-loading conditions and three combinations of blade pitch and rotor speed. A split-film total-vector anemometer was used to measure the three components of the wake-induced velocity. The data from the anemometer were sampled at blade azimuth angles of $\psi = 0$, 45, 90, and 135 deg for each rotor revolution. The wake-induced velocity was processed to generate the time-averaged values for each station along the wake radii at various distances below the rotor disk.

As shown by He and Goericke [21], empirical wake-decay parameters were needed to improve the downwash correlations with the measured data by using a potential-based finite-state dynamic wake model. Because the current model is based on the first-principle physics law (i.e., the Navier–Stokes equation in vorticity form), it should be beneficial to show that it can automatically capture the physical wake-decay effect without introducing any ad hoc empirical parameters.

Figure 2 shows the comparisons of the predicted time-averaged downwash with the measured data at $\psi = 0$ deg at three different vertical stations downstream of the rotor wake: $z = -0.1R$, $-0.15R$, and $-1.0R$. During the simulation, the rotor operated at a tip speed of 450 ft/s and was trimmed to the same mean thrust coefficient as that in the experiment: $C_T = 0.0040$. Each plot in Fig. 2 represents a variation of the time-averaged downwash along the radial direction and at a different vertical positions. From Fig. 2, it can be seen that the predicted wake downwash variation agrees well with the measured data at all of the vertical locations examined ($z/R = -0.1, -0.5$, and -1.0). The measured downwash profile showed that the rotor wake quickly contracts around $r/R = 0.8$ after leaving the rotor plane. The quick contraction of the rotor wake was accurately captured by using the vortex particle model, as indicated by the excellent agreement at this vertical station ($z/R = -0.1$). The measurement also indicated that as the wake travels further downstream, the strength of the tip vortex decays and the wake becomes more diffused. As shown in the figure, the predicted downwash at the far wake also exhibits excellent qualitative correlation with the measurement, which means that the wake decay and diffusion were captured well.

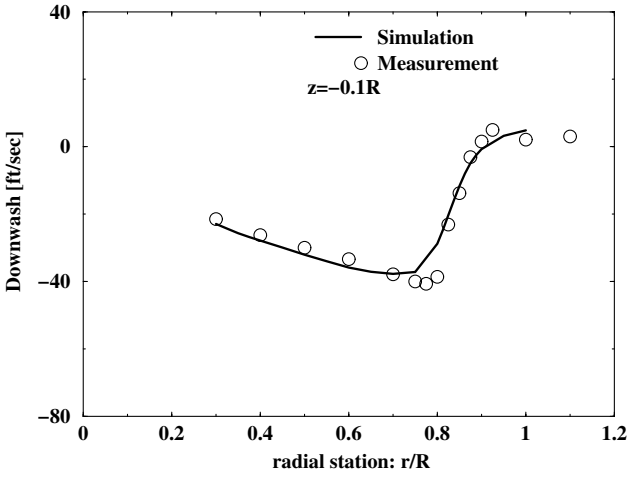

a) z = -0.1R

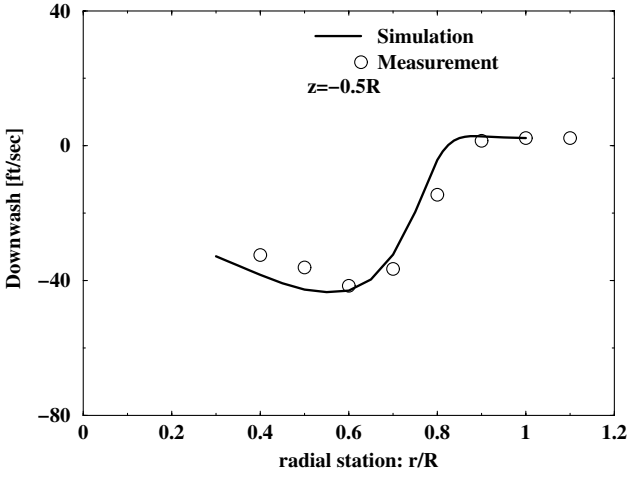

b) z = -0.5R

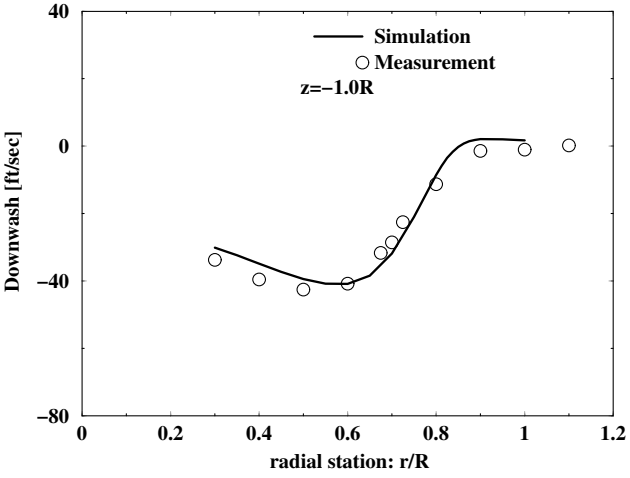

c) z = -1.0R

Fig. 2 Comparison of predicted rotor wake downwash with measured data for a full-scale isolated rotor in hover, $C_T = 0.0040$.

To gain further insight into the rotor wake dynamics in a hover condition, Fig. 3 presents the wake vorticity contour over a vertical

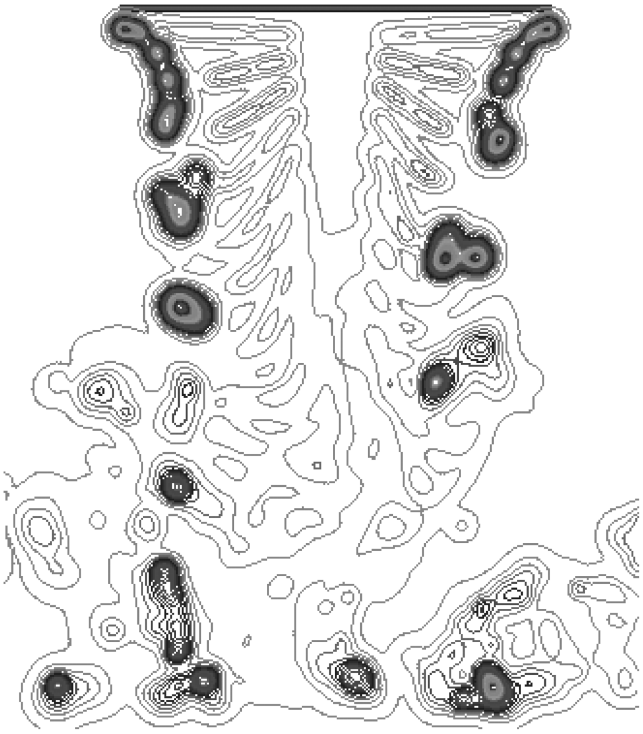

Fig. 3 Predicted rotor wake vorticity contour over a vertical plane passing through the rotor hub center of a two-bladed full-scale rotor in hover, $C_T = 0.0040$.

plane passing through the rotor hub center. As shown, the predicted rotor wake quickly contracted immediately below the rotor plane and a pair of strong tip vortices was developed along the contracted surface, which confirms the downwash variation, as shown in Fig. 2a. Figure 3 also demonstrates that the tip vortices exhibited a symmetric pattern initially and quickly became asymmetric when convected further downstream. In the far wake, the wake became more diffused and the wake mutual interactions caused the tip vortices to form the vortex pairing instability, which agrees with the phenomena observed from the experimental tests [22].

B. Rotor Wake Dynamics in Forward Flight

To further validate the viscous vortex particle model, the prediction accuracy of the current model for rotor wake dynamics in forward flight was investigated. Simulations were carried out for two isolated rotor systems at different forward-flight speeds, and the predicted wake-induced downwash were compared with available measured data.

The first case studied was a two-bladed isolated rotor at a relatively low advance ratio of $\mu = 0.095$. Heyson and Katzoff [23] measured the time-averaged downwash at different sampling planes below and downstream of the rotor plane. The rotor system had a teetering configuration with two untwisted and untapered blades. The rotor operated at a mean thrust coefficient of $C_T = 0.0032$ and a tip speed of $V_{\text{tip}} = 500$ ft/s.

Figure 4 presents snapshots of the predicted rotor wake structure displayed in terms of the vorticity isosurfaces. As shown, after the rotor rotated one revolution (Fig. 4a), the tip vortices that were trailed behind the two blades started to tangle around each other at the downstream location. This process was continued and an initial starting vortex bundle was formed, due to the mutual interactions of the tip vortices after two rotor revolutions (Fig. 4b). As the rotor continued to rotate, the tip vortices started to roll up along the rotor advancing and retreating sides, slightly after they left the rotor plane (Fig. 4c). The rolled-up tip vortices convected toward the downstream, together with the initial starting vortex bundle, as shown in Figs. 4d and 4e. After ten rotor revolutions (Fig. 4f), the starting vortex bundle was convected to three rotor radii away from the rotor plane and the fully rolled-up vorticity structure was well developed, which is very similar to the horseshoe-type vortex observed behind a fixed-wing aircraft. The visualizations in Fig. 4 demonstrated that the current model can preserve the concentrated rotor vorticity structure for a significantly long period of time, which is crucial to accurately predict the rotor interference on the airframe. An accurate prediction of rotor vorticity field is also essential for simulation of multiple-aircraft aerodynamic interaction and aircraft interaction with other external objects such as a ship deck and the ground.

In Fig. 5, the predicted rotor downwash at four x-cut planes ($x/R = -0.5$, 0.0, 0.5, 1.07 along the freestream direction) and different z (vertical) locations below the rotor plane were compared with the available measured data. During the simulation, the rotor was trimmed to the same thrust ($C_T = 0.0032$) and operating conditions as those in the experiment. Each plot in the figure corresponds to the correlations at a different x-cut plane along the freestream direction. There are three curves in each plot, which represent the downwash variation along a line parallel to the rotor Y axis (lateral axis) and formed by the specified x-cut plane and the z-cut plane in the rotor hub reference frame (Fig. 1).

From Fig. 5a, which shows the correlation at $x/R = -0.5$ (one-half rotor radius ahead of the rotor hub center), it can be seen that the downwash variation along the rotor Y axis is very smooth. This can be explained by the fact that the tip vortices from the two blades have not been fully rolled up at this specified location (Fig. 4f). However, for the locations at the rotor hub center and downstream of the hub center, the downwash variation shows a strong nonlinearity around both the advancing and retreating sides of the rotor plane, which implies strong rolled-up tip vortices and is consistent with the vorticity structure visualizations as presented in Fig. 4. In addition, the simulation results correlated well with the measured data at almost all the sampling planes except for $x/R = 1.07$.

As shown in Fig. 5d, the magnitude of the predicted downwash variation is slightly larger than the measured data and the region between the downwash peaks is narrower than that observed in the experiment, which means that the simulated rolled-up tip vortices are closer to each other than those in the experiment. This may be explained by the fact that the interference and diffusion introduced by the rotor shaft and the upstream measurement apparatus were not included in the current study.

Another validation case studied was the time-averaged downwash predictions and comparisons with the measured data taken at the U.S. Army/NASA Langley Research Center (LaRC) [24,25] facility for a model rotor in a forward-flight condition. Experiments were conducted using a four-bladed articulated rotor with both rectangular and tapered platform blades and at several different advance ratios. For the current study, the attention was focused on the rotor with a rectangular blade tip that operated at a mean thrust coefficient of 0.0064 and an advance ratio of $\mu = 0.23$. Figure 6 shows the predicted downwash distribution across the rotor disk plane. For comparison, the measured data were also superimposed on the plots.

Figures 6a and 6b show the downwash variation along the rotor longitudinal and lateral axes, respectively. It can be observed that the measured data displayed a strong upwash on the front part of the rotor disk and a strong downwash on the rear part of the rotor disk. This downwash variation can result in a very large longitudinal inflow gradient, which is essential to the rotor dynamics simulation in forward flight. Very impressively, the current vortex particle simulation captured these phenomena well in terms of both the magnitude and distribution. The predicted lateral inflow variation also correlated well with the measured data, especially near the blade tip region, in which most of the current potential-flow-based methods usually fail to do a good job. Some discrepancies existed between the simulation results and the measured data near the blade root region, which may be improved by including the effect of the pylon and the fuselage in the modeling.

In Figs. 6c and 6d, the predicted rotor downwash variation along the rotor azimuth when compared with the measured data at two different rotor radial stations: $r = 0.40R$ (inboard) and $r = 0.90R$ (blade tip). As shown, the simulation predictions at the blade tip

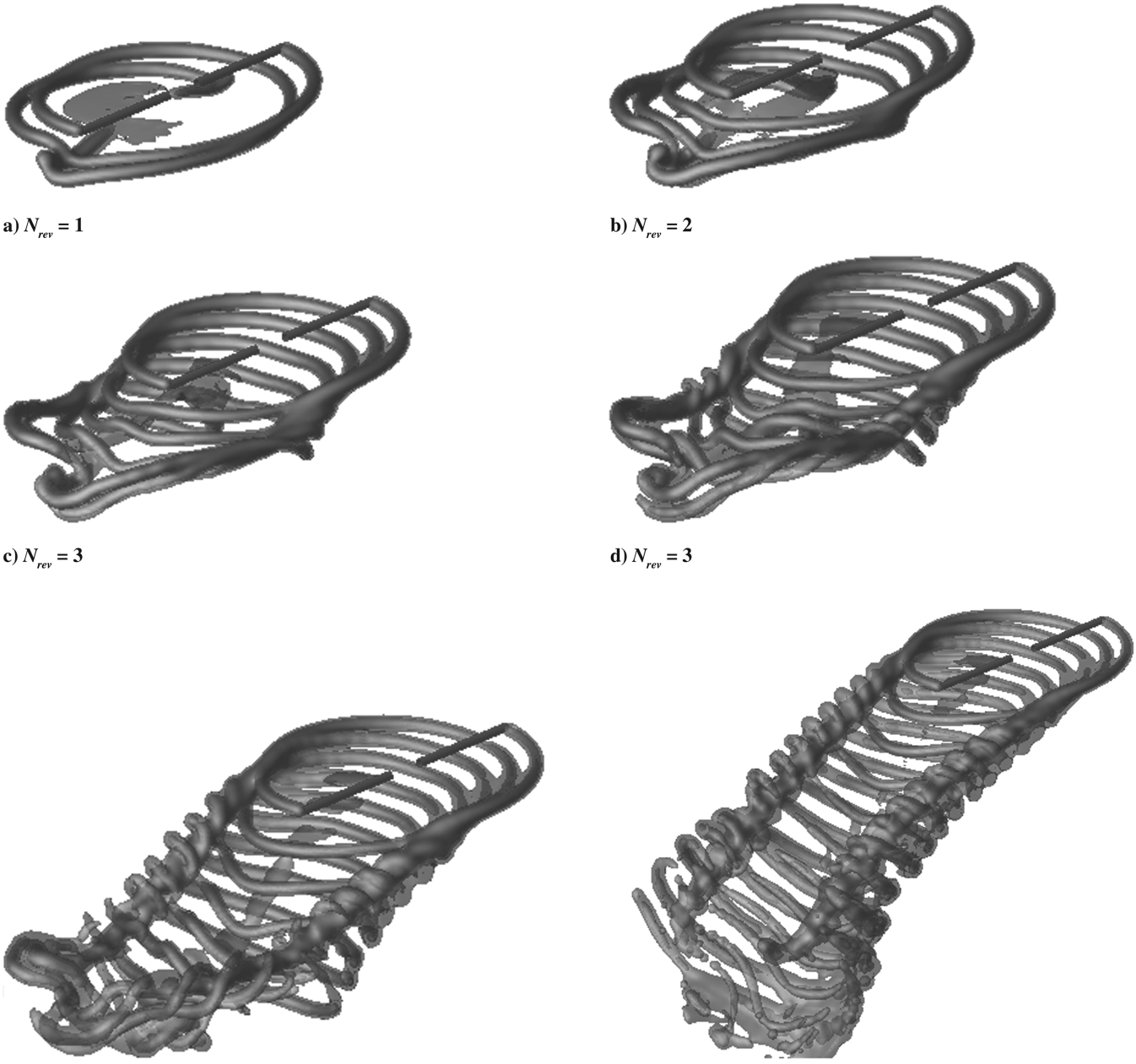

a) $N_{rev} = 1$ **b)** $N_{rev} = 2$ **c)** $N_{rev} = 3$ **d)** $N_{rev} = 3$ **e)** $N_{rev} = 6$ **f)** $N_{rev} = 10$

Fig. 4 Simulated rotor wake vorticity isosurfaces at different time instants for a two-bladed isolated rotor at an advance ratio of $\mu = 0.095$.

region ($r = 0.90R$) correlated well with the measured data. Both the magnitude and the azimuthal regions of the local strong upwash on the front part of the rotor disk as observed in the experiment were correctly captured. For the inboard station ($r = 0.40R$), there are some discrepancies between the simulation and the measured data, but the overall qualitative correlations are still good. Again, the lack of a pylon or fuselage in the simulation may be the cause of these discrepancies.

C. Rotor Dynamic Response to a Ramp Collective Input

In the previous validation cases, the rotor wake variation during a trimmed flight condition was studied, mainly by comparing the time-averaged downwash on and off the rotor disk with available measured data. When a helicopter is carrying out maneuvers or transitioning between different flight regimes, the rotor blades experience transient response, and therefore the characteristics of the trailed- and shed-vorticity variations are much more complicated. Adequately capturing the complicated unsteady vortex dynamics is imperative for the transient-response analysis of rotorcraft, which directly influences the analysis of vehicle controllability and stability. In this section, the rotor wake dynamics during a rapid increase in the collective pitch control were studied by using the developed vortex particle model. The study focused on the unsteady vorticity buildup, the rotor inflow development, the blade flapping, and the rotor thrust responses for a three-bladed articulated rotor in hover. The unsteady inflow, the blade flapping, and the thrust variations were measured for different rotor collective ramp inputs [26]. In this study, the rotor responses to two different increases of rotor collective pitch profiles were studied. Figure 7 shows the rotor collective changes from 0 to 12 deg at two different rates of 200 and 48 deg/s , respectively.

The rotor responses to a ramp collective pitch input of 12 deg at a rate of 200 deg/s were studied first. During the simulation, the rotor was rotating at the given speed and the initial collective pitch setting was zero. The specified collective pitch control profile (Fig. 7) was then applied and the corresponding developments of the rotor wake, the unsteady induced inflow, the rotor thrust, and the blade flapping angle were recorded and compared with the available measured data.

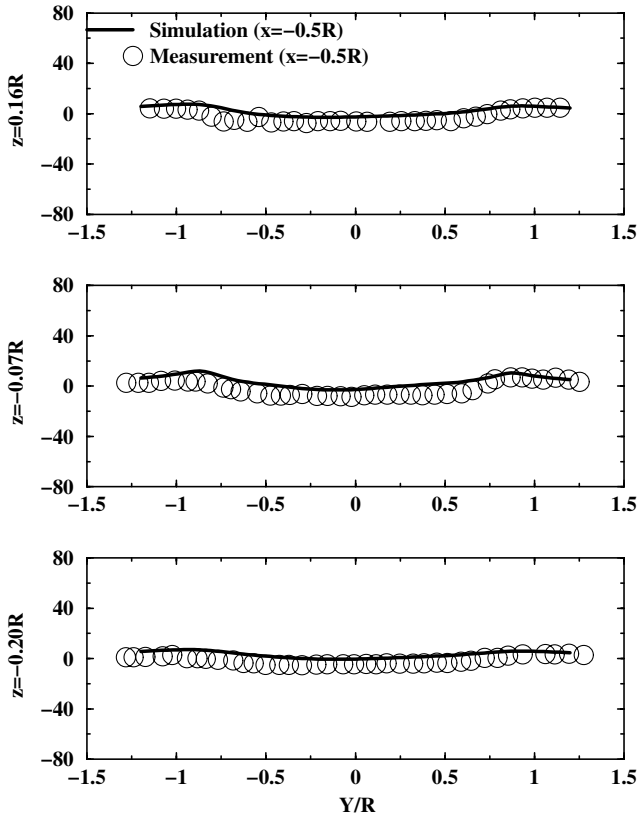

a) x / R = -0.5

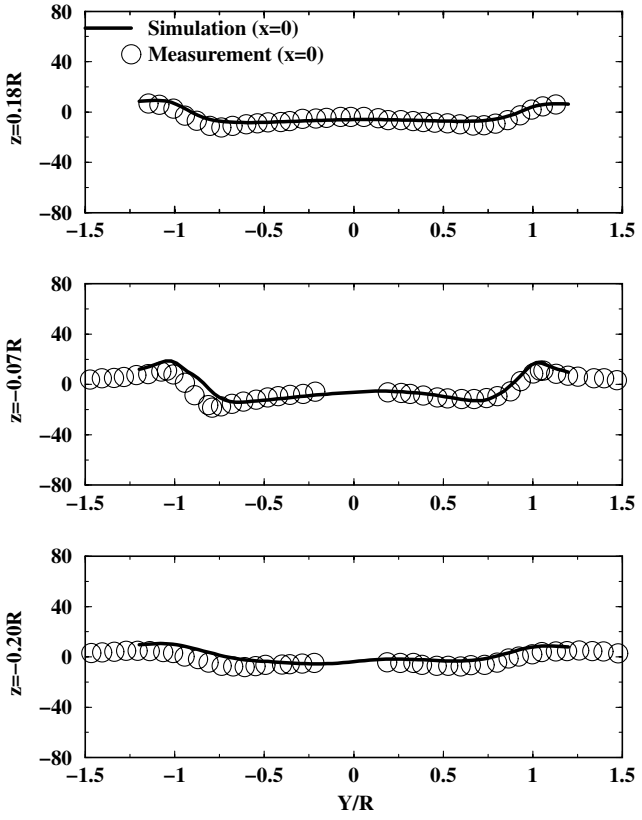

b) x / R = 0

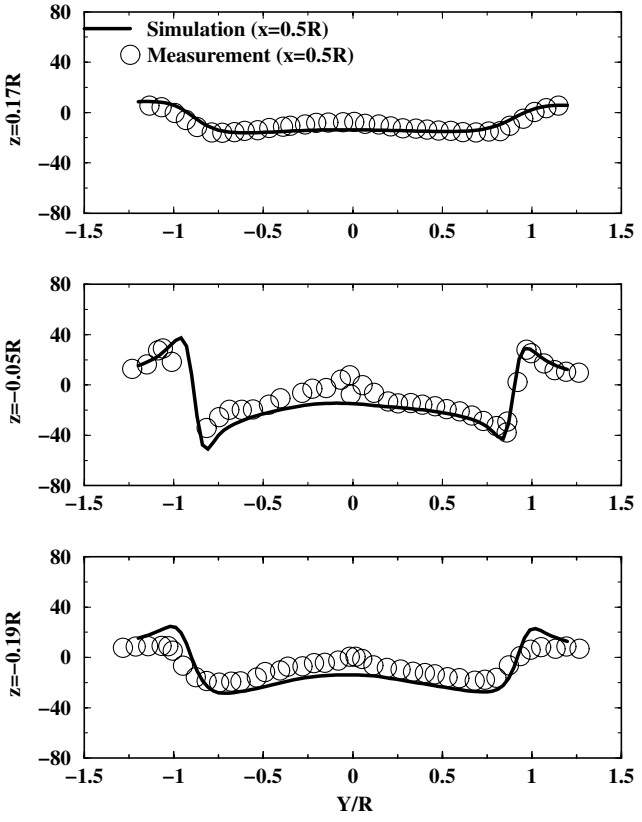

c) x / R = 0.5

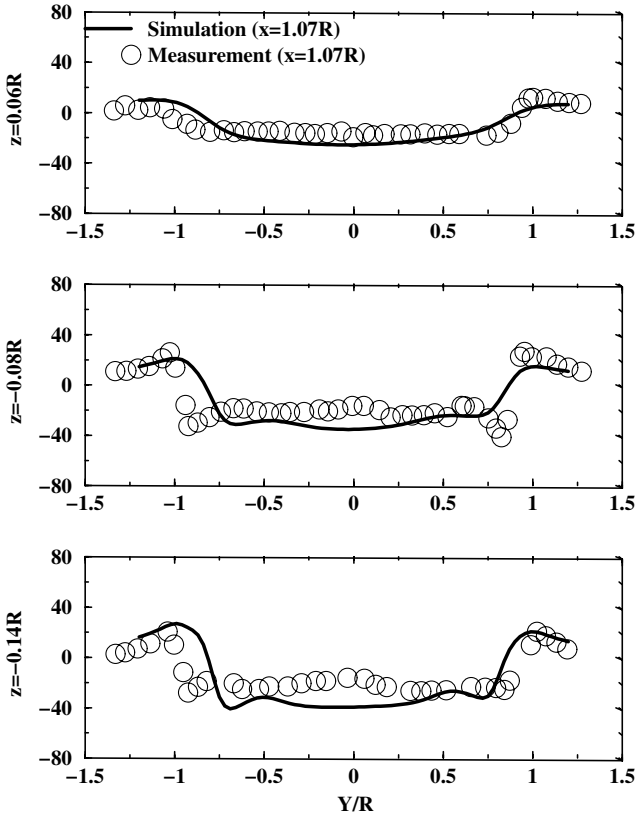

d) x / R = 1.07

Fig. 5 Comparison of predicted rotor downwash with measurement at different vertical planes for a two-bladed isolated rotor at an advance ratio of $\mu = 0.095$ and a thrust coefficient of $C_T = 0.0032$.

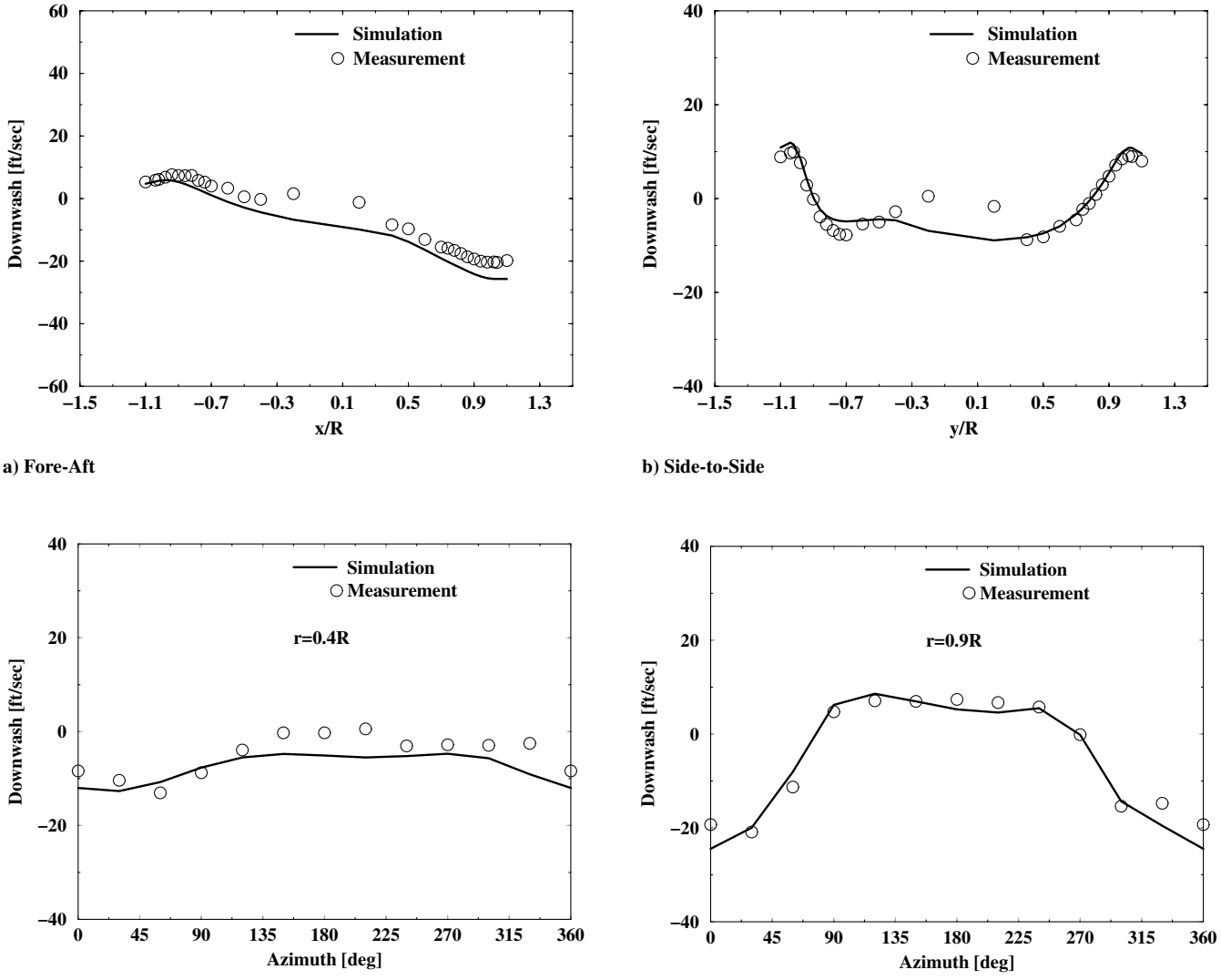

a) Fore-Aft

b) Side-to-Side

c) $r/R = 0.4$

d) $r/R = 0.9$

Fig. 6 Comparison of predicted downwash with the LaRC measurement for a four-bladed isolated rotor at a thrust coefficient of $C_T = 0.0064$ and an advance ratio of $\mu = 0.23$.

Figure 8 presents the snapshots of the predicted wake structure, expressed in terms of vorticity contours on a vertical plane passing through the rotor hub center. As shown in Fig. 8a, there are two initial vorticity bundles formed: one near the blade tip and one near the root.

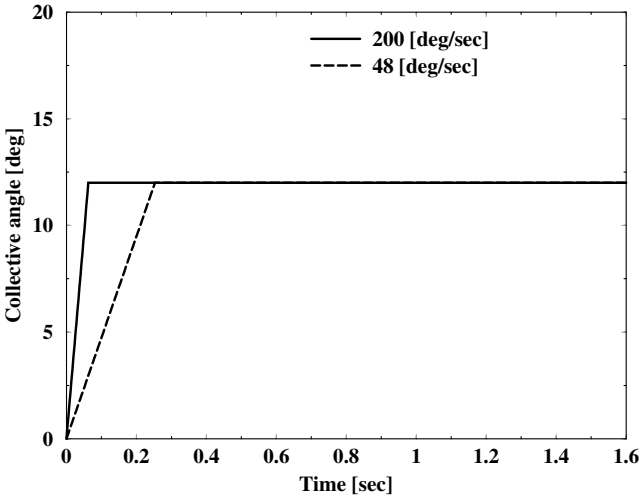

Fig. 7 Profiles of the collective ramp inputs.

As the rotor rotates, the initial tip vorticity bundles convect downward, whereas the root vortices convect upward, which is caused by the mutual interactions of the tip and root vortices (as verified by the unsteady inflow at the root and tip in Fig. 9a). After a few rotor revolutions, the rolled-up tip vortices formed an initial helical tip-vortex structure and convected further downstream (Figs. 8e and 8f).

The rotor responses to the given increase in collective pitch are presented in Fig. 9. For validation purposes, the corresponding measured data are superimposed on the plot. As shown, Figs. 9a and 9b are the unsteady rotor-induced inflow at different radial stations and the derived effective mean rotor inflow, respectively. The oscillation phenomena of the induced inflow observed in the simulation have a characteristic of $3/\text{rev}$, which is fundamental to a three-bladed rotor system. It can be observed that there is an initial upwash at the blade root ($r = 0.30R$) and a downwash at the blade tip region ($r = 0.9R$), which explains the initial movement of the tip and root vortices, as shown in Fig. 8. In addition, the predicted effective mean inflow correlates very well with the measured data, as demonstrated in Fig. 9b.

Similarly, Figs. 9c and 9d present the developments of the corresponding rotor thrust and blade flapping dynamics, respectively. It can be observed from the measured data that both the rotor thrust and the blade flapping angle overshoot almost 100% when compared with their steady-state values, which is caused by the

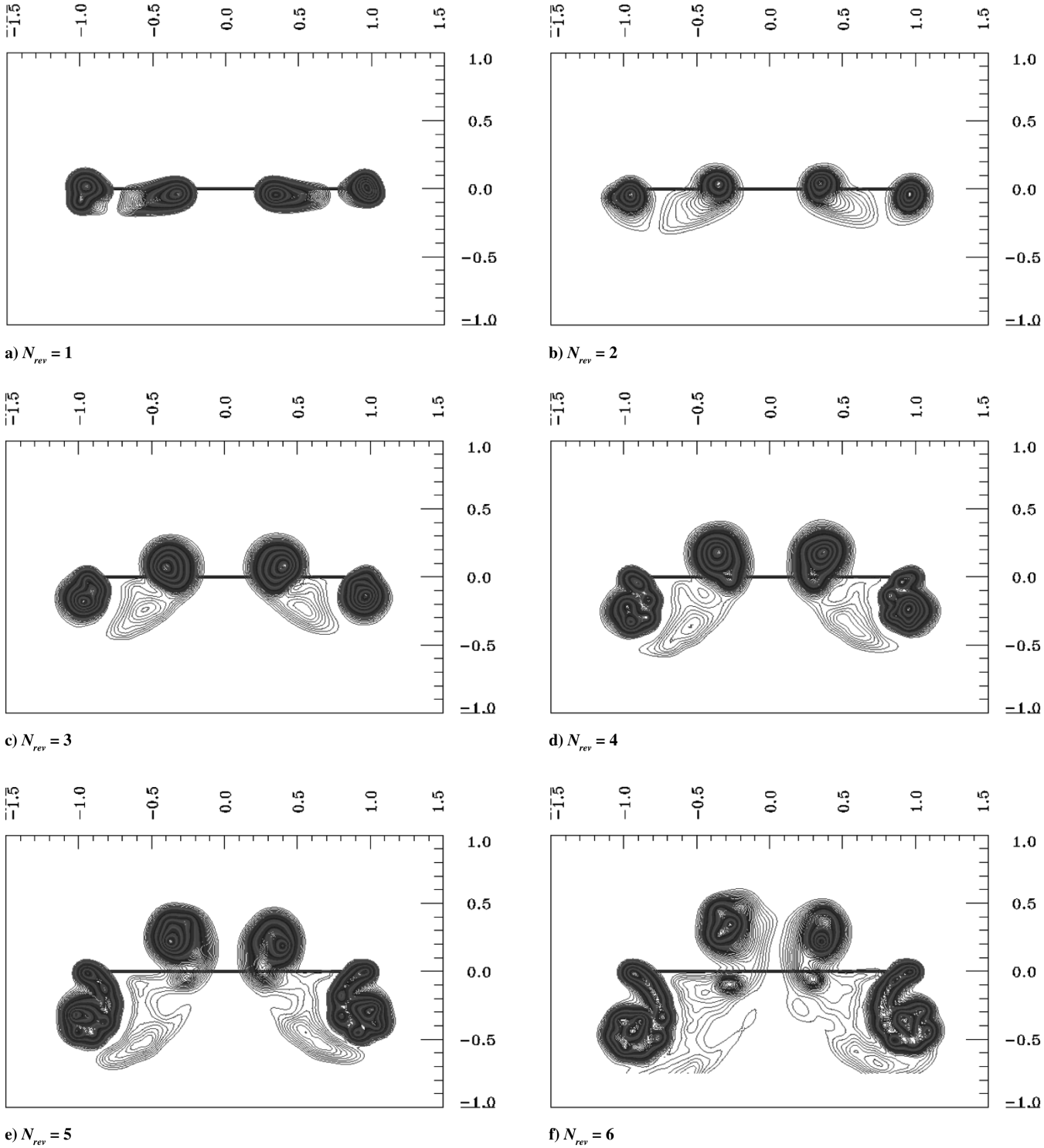

a) $N_{rev} = 1$ b) $N_{rev} = 2$

c) $N_{rev} = 3$ d) $N_{rev} = 4$

e) $N_{rev} = 5$ f) $N_{rev} = 6$

Fig. 8 Snapshots of the predicted wake vorticity contours on a vertical plane passing through the rotor hub center for a ramp collective input of 12 deg and at a rate of 200 deg/s from hover.

delays in the rotor-induced inflow buildup in following the rapid increase in the rotor collective control. As shown, the predicted rotor thrust matches well with the measured data in both the variation trend and the magnitude of the overshoot (Fig. 9c). The simulated blade flapping captures the time of the flapping overshoot, whereas the magnitude was slightly underpredicted. For both the thrust and the blade flapping responses, the steady-state values agree very well with the measurement.

To further validate the developed model for unsteady rotor wake dynamics, the responses of the same rotor to a slower ramp input at a rate of 48 deg/s (Fig. 7) were simulated, and the corresponding results are given in Fig. 10, including comparisons with the available measured data. Conclusions similar to those from Fig. 9 can be drawn.

V. Sensitivity Study of Modeling Parameters

In this section, the effects of modeling parameters on the simulation fidelity were investigated through parametric studies. The following particle modeling parameters were evaluated: 1) wake cutoff distance r_{cut}, 2) time-step size (or number of steps in one rotor revolution) NAZ, 3) overlapping parameter c_σ, and 4) resolution parameter h_{res}.

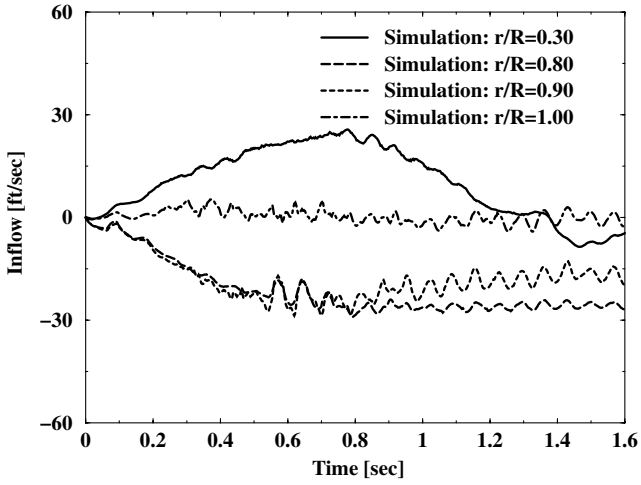

a) Inflow at different r/R

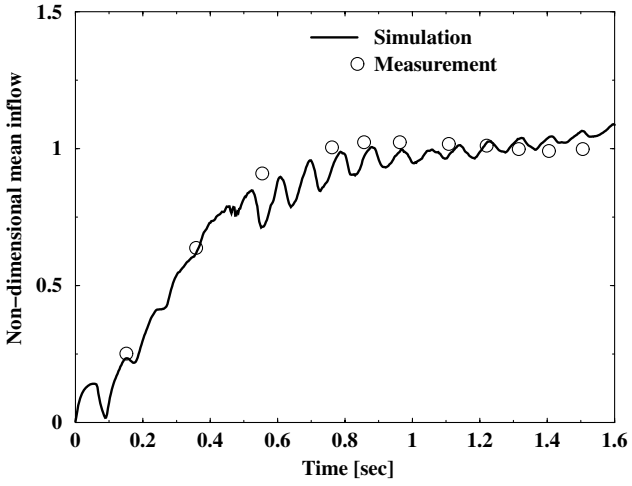

b) Mean inflow

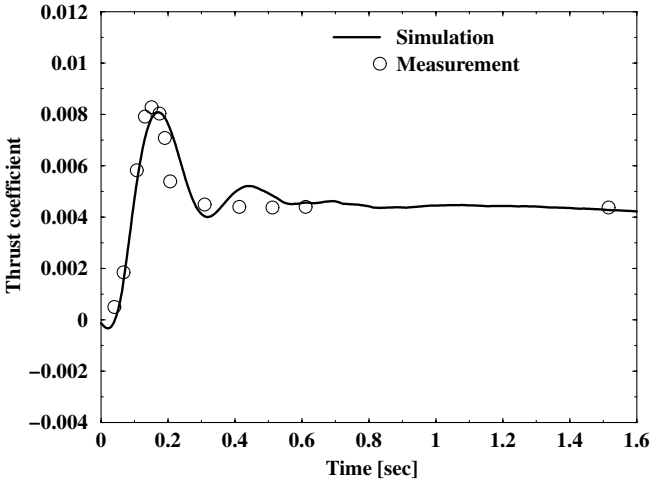

c) Rotor thrust

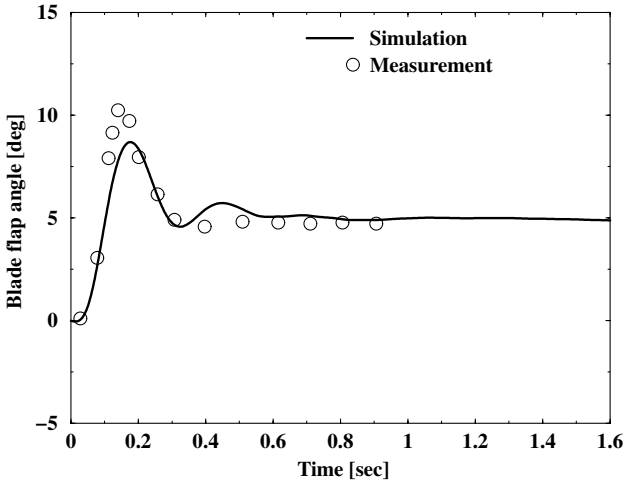

d) Blade flapping

Fig. 9 Predicted rotor responses to a ramp collective input of 12 deg and at a rate of 200 deg/s from hover.

Both the overlapping parameter c_σ and resolution parameter h_{res} determine the vortex particle smoothing parameter $\sigma = c_\sigma h_{\text{res}}$ used in the Gaussian distribution [Eq. (3)]. During the sensitivity study of the preceding modeling parameters, a set of nominal values of $c_\sigma = 1.3$, $h_{\text{res}} = 0.025R$, $r_{\text{cut}} = 3.0R$, and $NAZ = 96$ was used as a baseline. The modeling parameters were perturbed one by one to examine the sensitivity of the simulation results to the specified parameter. Because the rotor-induced inflow (downwash) is the most important and direct measure of the influence of wake dynamics on rotor aerodynamics, the inflow variation across the rotor disk predicted with different modeling parameter values was used as the sensitivity criteria in the current study.

The effect of the rotor wake cutoff distance r_{cut} was first studied. The wake cutoff-distance parameter determines the far-wake distance from the flowfield area of interest (e.g., the rotor disk), beyond which the vortex particles are dropped for computational efficiency. In this scenario, the full-scale isolated rotor example in a hover condition, as shown in Sec. IV.A, was used. The rotor wake was cut off at three different distances: $r_{\text{cut}} = 2.0R$, $3.0R$, and $4.0R$. Figure 11 shows the downwash distributions at two vertical sampling planes ($z = -0.1R$ and $-0.5R$) predicted with different wake cutoff distances, including comparisons with the measured data. It can be observed that all the simulation results have comparable correlations with the measured data, which indicates that the sensitivity of the simulation to the wake cutoff-distance parameter is not significant, provided that $r_{\text{cut}} \geq 2.0R$ in this case.

The effect of simulation time-step size, which is equivalent to the number of steps in one rotor revolution (NAZ), was studied next. As discussed in the Vorticity Source Generation section, the new vortex particles were generated along a mapping surface spanned by the blade positions at two consecutive time steps to ensure overlapping between new vortex particles. An advantage of this approach is that it alleviates the simulation sensitivity to the simulation step size. The LaRC rotor in forward flight (Sec. IV.B) was used here to study the effect of the time-step size on the rotor inflow predictions.

Figure 12 presents the downwash variations along the rotor longitudinal and lateral axes, predicted with different values of NAZ, including comparisons with the measured data. It can be seen that even though the simulation results exhibit a certain sensitivity to the NAZ parameter, the fundamental trends of the nonlinear longitudinal and lateral inflow variations were well captured, even with a large step size of 15 deg ($NAZ = 24$), when compared with a very small step size of $NAZ = 192$. Overall, the simulation results predicted with different integration time-step sizes correlate qualitatively well with measured data, and the difference between different modeling parameters is that they predicted somewhat different downwash magnitudes.

Similarly, the LaRC rotor in forward flight (Sec. IV.B) was also used for the sensitivity study of the particle smoothing parameter, which is determined by the overlapping parameter c_σ and the resolution parameter h_{res}. For the overlapping parameter c_σ, a minimum value of 1.0 is required to ensure the convergence of the

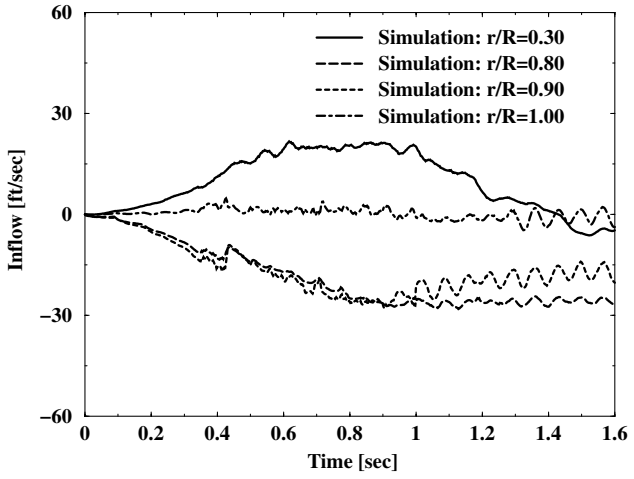

a) Inflow at different r / R

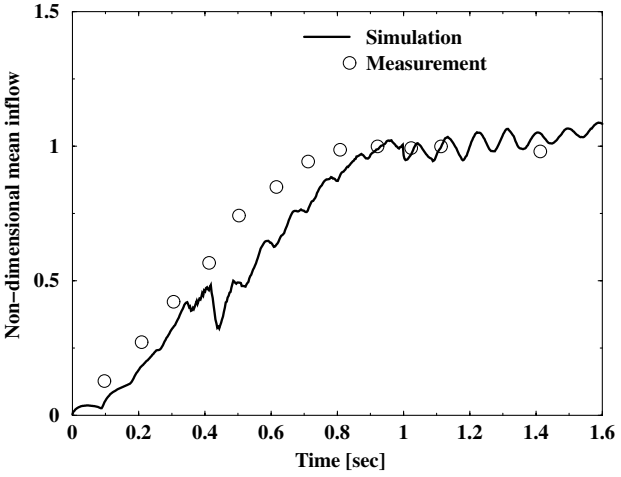

b) Mean inflow

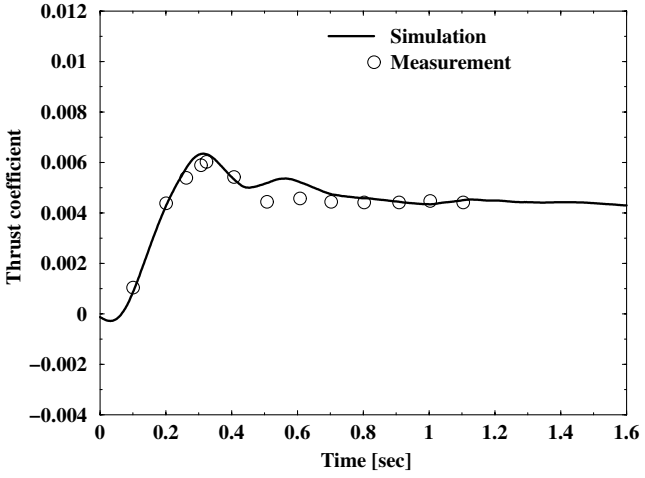

c) Rotor thrust

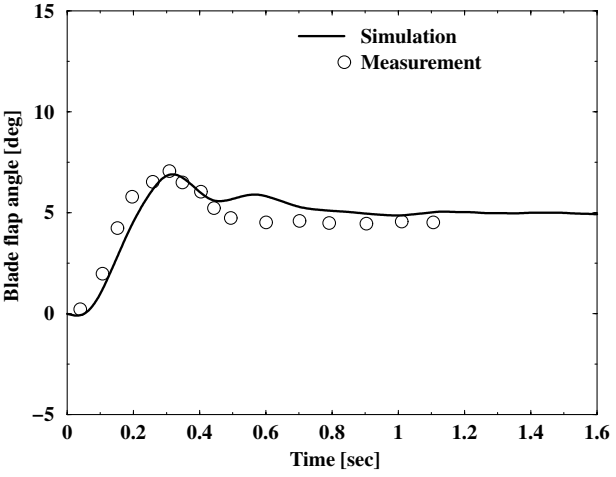

d) Blade flapping

Fig. 10 Predicted rotor responses to a ramp collective input of 12 deg and at a rate of 48 deg/s from hover.

overall vortex particle method [4,18]. The resolution parameter h_{res} governs the minimum flowfield resolution resolved. Figure 13 presents the rotor longitudinal and lateral downwash variations predicted with three different overlapping parameters: $c_\sigma = 1.0$, 1.3, and 2.0. Similarly, Fig. 14 shows the predicted downwash variations for three different resolution parameters: $h_{\text{res}} = 0.0125R$, $0.025R$, and $0.05R$. As shown, all of the simulation results predicted with different overlapping and resolution parameters have comparable correlations with the measured data, which indicates that there is no significant sensitivity issue to the smoothing parameters.

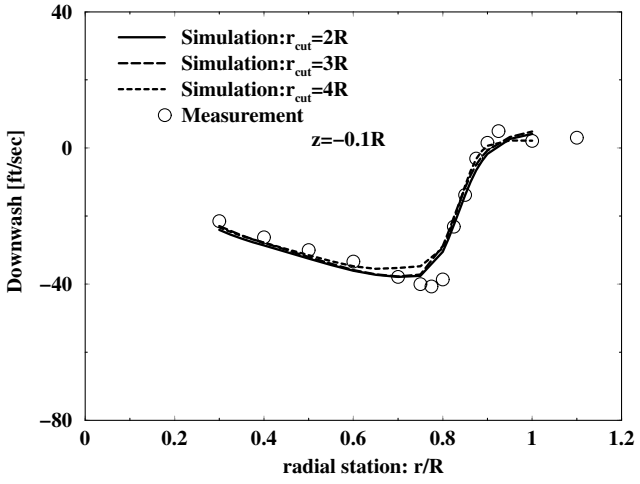

a) z / R = -0.1

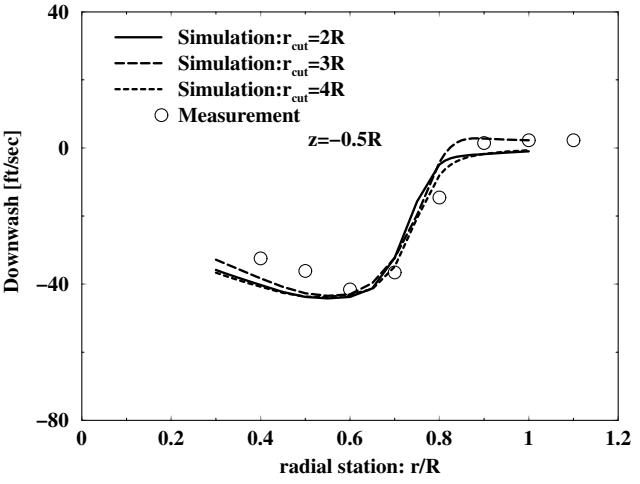

b) z / R = -0.5

Fig. 11 Effect of the rotor wake cutoff distance r_{cut} on the downwash predictions for the full-scale isolated rotor in hover condition $C_T = 0.0040$.

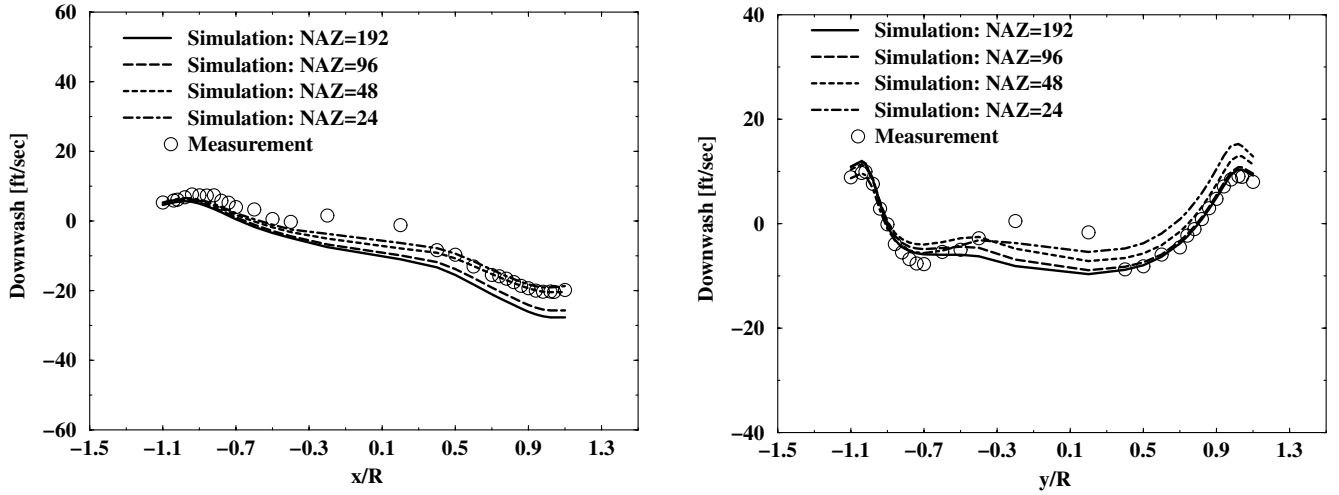

a) Fore-aft b) Side-to-side

Fig. 12 Effect of time-step size on the rotor downwash predictions for the LaRC rotor at forward-flight condition $\mu = 0.23$ and $C_T = 0.0060$.

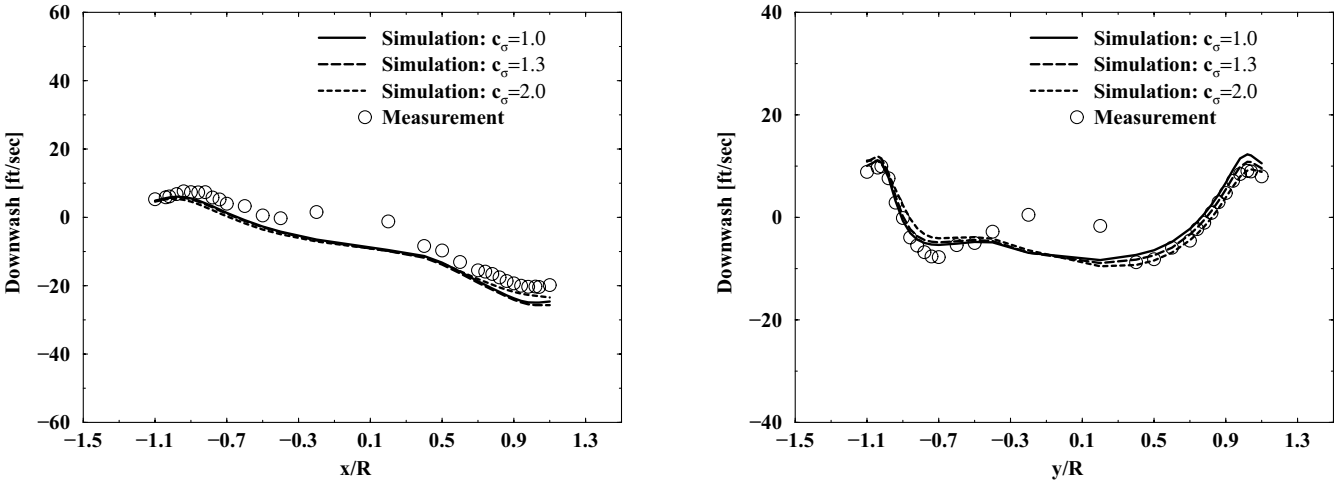

a) Fore-aft b) Side-to-side

Fig. 13 Effect of the overlapping parameter c_σ on the rotor downwash predictions for the LaRC rotor at a forward-flight condition, $\mu = 0.23$, $C_T = 0.0060$.

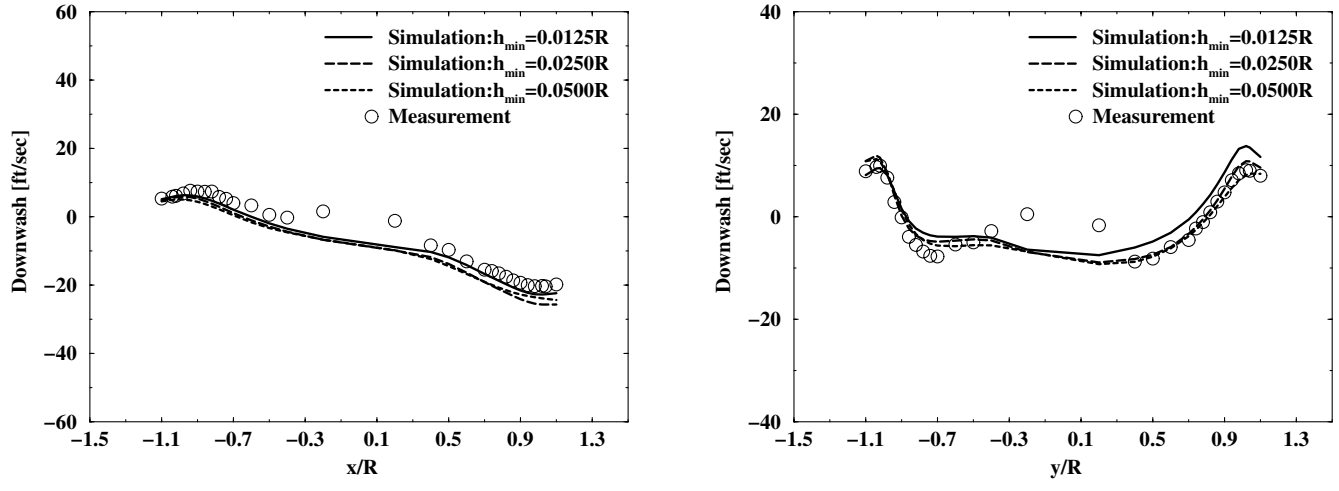

a) Fore-aft b) Side-to-side

Fig. 14 Effect of the resolution parameter h_{res} on the rotor downwash predictions for the LaRC rotor at a forward-flight condition, $\mu = 0.23$, $C_T = 0.0060$.

VI. Conclusions

A first-principle physics-law-based (the incompressible Navier–Stokes equation) viscous vortex particle model has been successfully developed for modeling complicated rotor wake dynamics. Despite the high degree of nonlinearity of the rotor wake vorticity resulting from its strong self-interaction during the transportation, the numerical tests illustrated the robust solution convergence characteristics of the viscous vortex particle model when applied to the rotor wake simulation. The initial validation tests have shown the following:

1) The viscous vortex particle model can accurately simulate the rotor wake variation in both hover and forward flight. The vortex particle model captures the fundamental characteristics of the rotor wake vorticity interaction, such as the wake contraction and tip-vortex roll-up, without using any empirical modeling parameters, which the existing potential-flow-based free-vortex models rely on for solutions.

2) The viscous vortex particle model can adequately predict the physical wake diffusion in terms of the induced velocity decay, as shown in the correlations between the simulation results and the measured flowfield data for a full-scale rotor. Again, this is accomplished without any empirical ad hoc.

3) The unsteady rotor wake dynamics and the rotor responses to a rapid change in the rotor collective pitch control were accurately predicted with the current viscous vortex particle model when compared with the measured rotor responses for a full-scale rotor.

4) There is only a small set of modeling parameters used in the current viscous vortex particle model, and the sensitivity of the simulation fidelity to these modeling parameters is low.

In this study, the validations were performed using vorticity sources generated from a simple lifting-line blade element model. However, the viscous vortex particle model (VPM) developed here is formulated with a generic interface that enables it, with some additional development work, to couple with a more sophisticated CFD blade-airload module for high-fidelity blade-load calculation. For a coupled CFD/VPM solution, a CFD solver can be applied to compute the flowfield solution near the blade surfaces and provide the vorticity sources, and the viscous vortex particle model can effectively resolve the rotor vorticity transportation through the rotor flowfield with a significantly improved computational efficiency. With its accurate representation of rotor wake geometry and wake vorticity strength variation in accordance with fluid dynamics laws, the viscous vortex particle model can provide a high-fidelity analytical tool for rotor wake interference prediction under both steady and maneuvering flight conditions.

References

[1] Brown, R., "Rotor Wake Modeling for Flight Dynamics Simulation of Helicopter," *AIAA Journal*, Vol. 38, No. 1, 2000, pp. 57–63.

[2] Line, A., and Brown, R., "Efficient High-Resolution Wake Modelling Using the Vorticity Transport Equation," *60th Annual Forum of the American Helicopter Society*, AHS International, Alexandria, VA, June 2004, pp. 1025–1093.

[3] Saffman, P. G., *Vortex Dynamics*, Cambridge Univ. Press, New York, 1992.

[4] Cottet, G. H., and Koumoutsakos, P. D., *Vortex Methods: Theory and Practice*, Cambridge Univ. Press, New York, 2000.

[5] Leonard, A., "Computing Three-Dimensional Incompressible Flows with Vortex Elements," *Annual Review of Fluid Mechanics*, Vol. 17, 1985, pp. 523–559.

[6] Winckelmans, G., "Topics in Vortex Methods for the Computation of Three- and Two-Dimensional Incompressible Unsteady Flows," Ph.D. Thesis, California Inst. of Technology, Pasadena, CA, 1989.

[7] Ploumhans, P., and Winckelmans, G. S., "Vortex Methods for High-Resolution Simulations of Viscous Flow Past Bluff Bodies of General Geometry," *Journal of Computational Physics*, Vol. 165, No. 2, 2000, pp. 354–406. doi:10.1006/jcph.2000.6614

[8] Ploumhans, P., and Winckelmans, G. S., "Vortex Methods for Direct Numerical Simulation of Three- Dimensional Bluff-Body Flows: Applications to the Sphere at $Re = 300$, 500, and 1000," *Journal of Computational Physics*, Vol. 178, No. 2, 2002, pp. 427–463. doi:10.1006/jcph.2002.7035

[9] Merriman, B., "Particle Approximation," *Vortex Dynamics and Vortex Methods*, AMS Lectures in Applied Mathematics, Vol. 28, American Mathematical Society, Providence, RI, 1991, pp. 481–546.

[10] Gallic, S. M., "Deterministic Particle Method: Diffusion and Boundary Conditions," *Vortex Dynamics and Vortex Methods*, AMS Lectures in Applied Mathematics, Vol. 28, American Mathematical Society, Providence, RI, 1991, pp. 433–480.

[11] Barnes, J., and Hut, P., "A Hierarchical $\mathcal{O}(N \log N)$ Force-Calculation Algorithm," *Nature*, Vol. 324, No. 4, 1986, pp. 446–449.

[12] Dehnen, W., "A Hierarchical $\mathcal{O}(N)$ Force Calculation Algorithm," *Journal of Computational Physics*, Vol. 179, No. 1, 2002, pp. 27–42. doi:10.1006/jcph.2002.7026

[13] Pfalzner, S., and Gibbon, P., *Many Body Tree Methods in Physics*, Cambridge Univ. Press, New York, 1996.

[14] Warren, M. S., and Salmon, J. K., "A Parallel, Portable and Versatile Treecode," *Seventh SIAM Conference on Parallel Processing for Scientific Computing*, Society for Industrial and Applied Mathematics, Philadelphia, 1995, pp. 319–324.

[15] Salmon, J. H., Warren, M. S., and Winckelmans, G. S., "Fast Parallel Tree Codes for Gravitational and Fluid Dynamical N-Body Problems," *International Journal of Supercomputer Applications and High Performance Computing*, Vol. 8, No. 2, 1994, pp. 129–142.

[16] Greengard, L., and Rokhlin, V., "A Fast Algorithm for Particle Simulations," *Journal of Computational Physics*, Vol. 135, No. 2, 1997, pp. 280–292. doi:10.1006/jcph.1997.5706

[17] Cheng, H., Greengard, L., and Rokhlin, L., "A Fast Adaptive Multipole Algorithm in Three Dimensions," *Journal of Computational Physics*, Vol. 155, No. 2, 1999, pp. 468–498. doi:10.1006/jcph.1999.6355

[18] Eldredge, J. D., Leonard, A., and Colonius, T., "A General Deterministic Treatment of Derivatives in Particle Methods," *Journal of Computational Physics*, Vol. 180, No. 2, 2002, pp. 686–709. doi:10.1006/jcph.2002.7112

[19] Fritsch, F., and Carelson, R., "Monotone PieceWise Cubic Interpolation," *SIAM Journal on Numerical Analysis*, Vol. 17, No. 2, 1980, pp. 238–246. doi:10.1137/0717021

[20] Boatwright, D. W., "Measurements of the Velocity Components in the Wake of a Full Scale Helicopter Rotor in Hover," U.S. Army Air Mobility Research and Development Lab., TR 72-33, Fort Eustis, VA, Aug. 1972.

[21] He, C., and Goericke, J., "Modeling Enhancements for Physics-Based Simulation Validations," *61st Annual Forum of the American Helicopter Society*, AHS International, Alexandria, VA, June 2005, pp. 1082–1093.

[22] Landgrebe, A., "The Wake Geometry of a Hovering Helicopter Rotor and Its Influence on Rotor Performance," *Journal of the American Helicopter Society*, Vol. 17, No. 4, 1972, pp. 3–15.

[23] Heyson, H. H., and Katzoff, S., "Induced Velocities Near a Lifting Rotor with Nonuniform Disc Loading," NACA TR 1319, 1957.

[24] Elliott, J. W., Althoff, S. L., and Sailely, R. H., "Inflow Measurements Made with a Laser Velocimeter on a Helicopter Model in Forward Flight," Vol. 2, NASA TM-100542, Apr. 1988.

[25] Elliott, J. W., Althoff, S. L., and Sailely, R. H., "Inflow Measurements Made with a Laser Velocimeter on a Helicopter Model in Forward Flight," Vol. 3, NASA TM-100543, Apr. 1988.

[26] Carpenter, P., and Fridovich, B., "Effect of a Rapid Blade-Pitch Increase on the Thrust and Induced-Velocity Response of a Full-Scale Helicopter Rotor," NACA TN 3044, 1953.

J. Sahu
Associate Editor